Applied Catalysis B: Environmental 256 (2019) 117805

Contents lists available at ScienceDirect

Applied Catalysis B: Environmental

journal homepage: www.elsevier.com/locate/apcatb

MnO_x-decorated 3D porous C_3N_4 with internal donor–acceptor motifs for efficient photocatalytic hydrogen production

Minhua Ai[a,b], Jing-Wen Zhang[a,b], Ruijie Gao[a,b], Lun Pan[a,b], Xiangwen Zhang[a,b], Ji-Jun Zou[a,b,*]

[a] Key Laboratory for Green Chemical Technology of Ministry of Education, School of Chemical Engineering and Technology, Tianjin University, Tianjin 300072, China
[b] Collaborative Innovative Center of Chemical Science and Engineering (Tianjin), Tianjin 300072, China

ARTICLE INFO

Keywords:
Carbon nitride
3D porous structure
Salt template
Donor-acceptor system
Photocatalysis

ABSTRACT

Carbon nitride is an intriguing visible-light photocatalyst for H_2 production but suffers from low surface area and fast charge recombination. Here, we report a simple yet efficient approach to fine tune the porous structure, modify the electronic structure and carrier behaviors of C_3N_4 through in-situ growth of MnO_x by NaCl template-assisted strategy. This NaCl template method simultaneously constructs 3D porous structure for high surface area, induces Na coordination with N atoms and accompanying cyano group to form an internal donor-acceptor system for efficient charge transfer and separation. Along with the MnO_x growth, the band gap of C_3N_4 is narrowed for stronger visible light absorption and the conduction band level is negatively shifted for stronger reduction capability. Thus, the resulted C_3N_4 (MSCN) shows much improved activity of about 18 times higher than bulk C_3N_4 in photocatalytic hydrogen evolution reaction under visible light irradiation.

1. Introduction

Hydrogen is an ideal energy carrier that is the hope of sustaining the future energy demands [1]. Among the ways for producing hydrogen, photocatalysis based on semiconductors is a promising technology and enables directly convert solar energy for hydrogen production [2–4]. Carbon nitride (C_3N_4), as a conjugated polymeric semiconductor, is an intriguing visible-light photocatalyst with abundant resources, good thermal stability, suitable energy band structure, and tunable molecular structure. However, C_3N_4 commonly synthesized by polycondensation of nitrogen-rich organic precursors suffers from low surface area, uncontrollable structure and high electron-hole recombination rates. Various attempts have been made to boost the performance of C_3N_4, including construction of heterostructure [5–7], design of porous structure [4,8,9], modification of electronic structure by heteroatoms doping [10,11] or metal coordination [12,13] and grafting functional group [14]. Nevertheless, the activity of C_3N_4 is still restrained and more efforts are necessary to obtain more satisfactory activity.

C_3N_4 with flexible porous structure fabricated by hard or soft templating method can provide abundant active sites and a shorter charge diffusion distance for enhanced photocatalytic performance [15,16]. However, traditional template-based methods are not only time-consuming but also environmentally unfriendly because additional calcining or reagents are needed to remove templates. Recent studies have proved that chlorine salts (NaCl, KCl, etc) with high melting point is a green template that can be easily removed by dissolving in water, and suitable for large-scale production due to its low cost. Specially, such a chlorine salt can not only act as the growth template to tailor nanostructure but also modulate electronic structure by introducing donor-type metal coordination and concomitant acceptor-type cyano group in the synthesis [17–19]. Notably, simultaneously introducing donor and acceptor moieties into C_3N_4 framework can constitute a donor–acceptor (D–A) system which is believed to be an internal driving force for separation of charge carriers. Fan et al. [20] reported that copolymerizing urea with dibromo aromatics can construct intramolecular D-A copolymers in which the enhanced activity is obtained from the effective charge transfer transition from donor (N) in C_3N_4 to the incorporating acceptor (aromatic ring). Wang et al. [21] designed a bioinspired D-A system using a selenium and cyanamide-functionalized heptazine-based melon and obtained a high efficiency in charge separation and transfer. Other D-A systems such as triazine–heptazine-based copolymers [22], a NDI-based copolymer system [23] and D-π–A-π–D structured g-C_3N_4 [24] have been created to show much improved photocatalytic activity. Besides, cocatalyst is also effective to promote charge separation along facilitate reaction [25]. Noble metals, especially Pt with the lowest overpotential, are considered to be the best cocatalysts for proton reduction. Transition metal oxides (MO_x), like CoO_x [26] and MnO_x [27], as hole-trapping sites can effectively modulate holes to avoid

* Corresponding author at: Key Laboratory for Green Chemical Technology of Ministry of Education, School of Chemical Engineering and Technology, Tianjin University, Tianjin 300072, China.
E-mail address: jj_zou@tju.edu.cn (J.-J. Zou).

https://doi.org/10.1016/j.apcatb.2019.117805
Received 29 March 2019; Received in revised form 21 May 2019; Accepted 30 May 2019
Available online 31 May 2019
0926-3373/

recombination with electrons for improving the efficiency [28].

Based on above considerations, here we report our attempt to modify the electronic structure and carrier behaviors of C_3N_4 by using NaCl as template and in-situ growth of MnO_x, which results in increased surface area, enhanced visible light absorption and improved charge separation. NaCl not only acts as template for 3D porous structure but also takes part in constructing an internal donor-acceptor heterostructure by introducing donor-type Na ions and producing acceptor-type cyano groups via the NaCl-catalytic pyrolysis of tri-s-triazine units. Meanwhile, we prove that decoration of MnO_x on C_3N_4 can further promote charge separation and improve photocatalytic performance. As a result, the MnO_x-decorated 3D porous C_3N_4 with internal donor–acceptor motifs exhibits remarkably photocatalytic H_2 evolution activity of 18 times higher than bulk C_3N_4 under visible light. This work is expected to provide a strategy to modify the electronic structure and carrier behaviors of C_3N_4 for photocatalysis.

2. Experimental section

2.1. Materials

Dicyandiamide (DCDA), sodium chloride (NaCl) and triethanolamine (TEOA) were purchased from Aladdin Industrial Corporation. Manganese (II) acetate tetrahydrate was supplied by Tianjin Guangfu Fine Chemical Research Institute. All reagents used in this work were without further purification. Ultrapure Milli-Q water (> 18.2 MΩ cm) was used for all experiments.

2.2. Fabrication of catalysts

The MnO_x-decorated C_3N_4 photocatalyst (MSCN) was fabricated by a salt-template-assisted in-situ growth method as shown in Scheme 1. In the typical synthesis, 2.52 g dicyandiamide, 17.53 g NaCl as template (the molar ratio of DCDA: NaCl = 1:10) and 0.08 g manganese acetate were dissolved into 100 mL ultrapure water under continuous magnetic stirring for 12 h. The resulted solution was frozen in the refrigerator for 12 h and dehydration by freeze-drying for 24 h to obtain fluffy white powders. Next, they were calcined at 520 °C for 4 h with a ramping rate of 2 °C/min in argon. The obtained yellow or brown powders were filtered and washed with water for several times to remove NaCl sufficiently and then freeze-dried. The samples synthesized with various amounts of manganese acetate (0.04, 0.08, 0.16 and 0.32 g) were denoted as $MSCN_x$, where x represents the dosage of Mn precursor. The effect of calcination temperatures (at 500, 520, 550, 570 and 600 °C) on the activity of MSCN-X samples was also tested with the amount of manganese acetate defined as 0.08 g, where X represents calcination temperatures. Unless otherwise stated, the used sample for characterizations and reaction was $MSCN_{0.08}$ calcinated at 520 °C (marked as MSCN). For comparison, a sample (MCN) without NaCl and a sample (SCN) without manganese acetate were prepared using the same procedure. Besides, bulk C_3N_4 (BCN) was synthesized facilely by thermal polymerization of dicyandiamide at 520 °C for 4 h.

2.3. Characterizations

Scanning electron microscope (SEM) images were observed using a field-emission scanning electron microscope (Hitachi, S-4800). Transmission electron microscopy (TEM), high-resolution transmission electron microscopy (HRTEM) and elemental mapping were carried out using a Tecnai G^2 F-20 transmission electron microscope with a field-emission gun operating at 200 kV. The BET surface area was determined using N_2 adsorption/desorption isotherm measurements at −196 °C on a Micrometrics TriStar 3000 equipment and all samples were outgassed under vacuum at 150 °C for 8 h. X-ray diffractometer (XRD) patterns were recorded at a scanning rate of 7°/min using Bruker AXS D8 XRD equipped with Cu Kα radiation at 40 kV and 40 mA. FTIR spectra were measured on a Bruker Vertex-70 Fourier transform infrared spectrometer. X-ray photoelectron spectrum (XPS) analysis was conducted with a PHI-1600 X-ray photoelectron spectroscope equipped with Al Kα radiation. UV–vis diffuse reflectance spectra (UV–vis DRS) were obtained from a Hitachi F-4600 spectrometer equipped with a 60 mm diameter integrating sphere using $BaSO_4$ as reference. Photoluminescence (PL) spectra were measured by a Shimadzu UV-2600 with the excitation light at 325 nm. Time-resolved anisotropy decays were recorded on a FL3 system (Horiba Scientific, Edison, NJ) utilizing time-correlated single photon count. Na and Mn contents were determined by induced coupled plasma atomic emission spectroscopy (ICP9000 N + M, USA Thermo Jarrell-Ash Corp.).

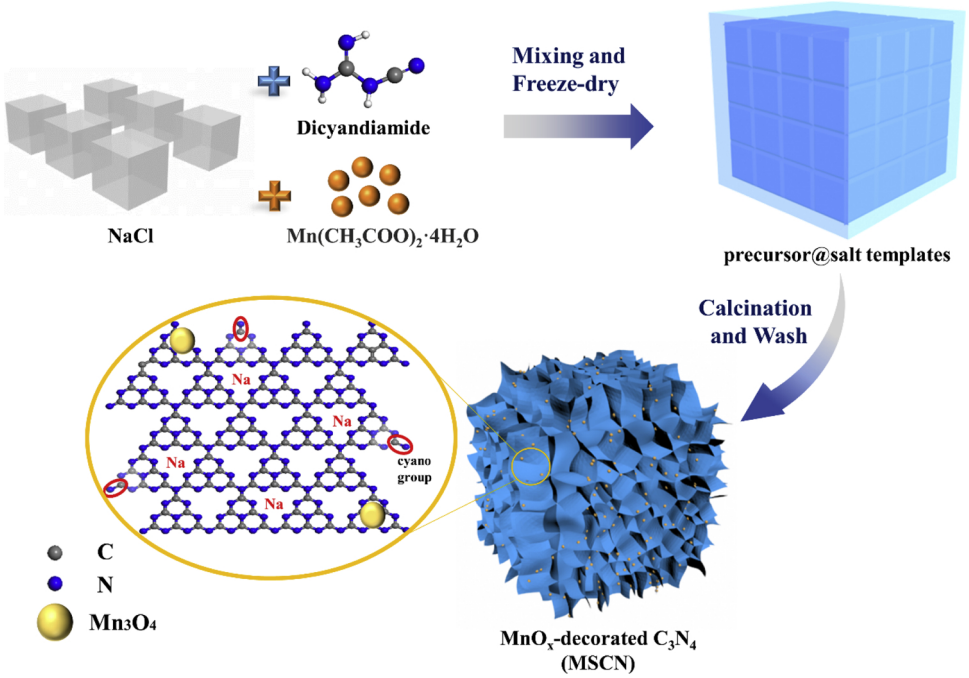

Scheme 1. Schematic illustration of fabrication of MnO_x-decorated 3D porous C_3N_4.

2.4. Photocatalytic tests

Photocatalytic hydrogen evolution was carried out in a 280 mL closed Pyrex top-irradiation vessel. Typically, 50 mg of photocatalyst was dispersed in 100 mL aqueous solution containing triethanolamine (10 vol%) as electron donor. 3 wt% Pt as co-catalyst was introduced by in-situ photodeposition with a 300 W Xeon-lamp for 2 h. The reaction system was completely evacuated to remove air prior to irradiation and then filled with Argon to 101 kPa. The reaction was conducted under a 300 W Xeon-lamp equipped with a 420 nm-cutoff filter, and the temperature was maintained at 0 °C. The evolved H_2 was analyzed by gas chromatography equipped with a thermal conductive detector (TCD) and a 5 Å molecular sieve column, using Ar gas as the carrier gas.

2.5. Photoelectrochemical measurements

The photoelectric performance tests were carried on a CHI 660B electrochemical system (Shanghai, China) using a standard three-electrode system with a working electrode, a platinum wire counter electrode, and an Ag/AgCl reference electrode. Na_2SO_4 (0.5 M) was used as the electrolyte solution. The working electrode was prepared by dip-coating as-prepared slurry on an F-doped tin oxide (FTO) glass electrode (1×1.5 cm^2) and drying it at 60 °C overnight. All the investigated working electrodes were of similar thickness. Electrochemical impedance spectroscopy (EIS) measurements were carried out at open circuit potential in the frequency range of 0.1–10^5 Hz. The transient photocurrent response tests were performed at 0.2 V bias potential versus Ag/AgCl.

3. Results and discussion

MSCN was fabricated by salt-templated synthesis as illustrated in Scheme 1. Typically, Dicyandiamide, manganese acetate as well as NaCl crystals were dissolved and then freeze-dried to produce a white precursor@salt templates powder (Fig. 1a). The mixture of dicyandiamide and manganese acetate perfectly cover the surface of NaCl crystals and self-assemble into a uniform cubic structure. The MSCN was obtained by calcining the precursor and dissolving NaCl in water. The morphology of prepared samples was checked by SEM and TEM images. In Fig. 1b, it is clearly that the opened pores size (*ca.* 1 μm) in MSCN is similar to the self-assembled crystal (Fig. 1a). Moreover, Fig. 1c clearly shows the staggered channel structure, which is consistent with SEM. The high-resolution TEM image in Fig. 1d shows the 0.247 nm interplanar spacing that can be assigned to the (211) spacing of Mn_3O_4 (*ca.* 15 nm) [29]. Without NaCl, the BCN and MCN present a severe stacked block structure which is unfavorable for light absorption and mass transfer (Fig. S1). The nitrogen adsorption–desorption isotherms (Fig. S2) show that all samples exhibit a typical IV curve, and the Brunauer-Emmett-Teller (BET) surface area of MSCN is 33.6 $m^2 g^{-1}$, which is significantly higher than that of BCN (13.9 $m^2 g^{-1}$) and MCN (10.4 $m^2 g^{-1}$), respectively. The increased surface area can be attributed to the 3D porous structure by salt-assisted strategy. The EDX-mapping shows the element distribution of MSCN including C, N, O, Na, Mn (Fig. 1e). Furthermore, Mn and O elements exhibit perfect overlap, confirming the formation of MnO_x, and Na is uniformly distributed in the C_3N_4 skeleton, indicating coordination within the C_3N_4 matrix. The accurate Mn and Na concentrations of MSCN measured by ICP-AES are 0.8 wt% and 6.4 wt% listed in Table S1.

BCN in Fig. 2a shows two characteristic peaks at 13.0° and 27.1° indexed to the (100) plane of periodic tri-s-triazine units and the (002) plane of aromatic systems of graphitic stacking, respectively [30]. For MSCN and SCN synthesized using NaCl template, the (100) peak almost disappear, mainly caused by the breaking of in-plane long-range order structure [31,32]. And broader and weaker (002) peak of MSCN shows a right shift (from 27.1° to 27.7°), suggesting the decrease of crystallinity and layer distance [33]. In addition, the absence of NaCl peak suggests that the sodium species are chemically coordinated with C_3N_4 host instead of isolated NaCl crystal, because Na ions prefer to combine with the lone pair of N atoms in form of Na-N bonds [34]. As for MCN and MSCN, no characteristic peaks of manganese oxides are observed, due to low content of MnO_x. However, when increasing the amount of manganese acetate (such as $MSCN_{0.32}$ in Fig. S3a), the diffraction peaks in good agreement with the standard monoclinic phase for Mn_3O_4 (JCPDS 24-0734) are observed (Fig. S3b) [35]. The Fourier transform infrared spectroscopy (FT-IR) were measured to analyze the chemical structures shown in Fig. 2b. All samples show the breathing mode of triazine units at 808 cm^{-1}, the feature of typical N = C–N hetero-aromatic rings stretches at 1200–1800 cm^{-1} and the broad peak of surface amine groups/absorbed water molecules at 2900-3500 cm^{-1}, indicating the original skeleton structure of C_3N_4 is essentially unchanged. Specifically, a new peak at around 2180 cm^{-1} of SCN and MSCN is assigned to the vibration of C≡N which results from the NaCl-catalytic pyrolysis of tri-s-triazine units [21]. The specific electron withdrawing property of C≡N will affect charge transfer and separation ability in C_3N_4 [36], and it can construct a donor–acceptor system when coupled with an electron-donating unit like donor-type Na ions.

The compositions and surface chemical states of fabricated samples were tested by X-ray photoelectron spectroscopy (XPS). The XPS survey spectra shown in Fig. S3 manifest the existence of C, N, O, Mn and/or Na in samples and the atomic ratio of each element analyzed by XPS of listed in Table S1. In the C 1s spectrum (Fig. 3a) there are three peaks at 288.3, 286.7 and 284.8 eV, corresponding to sp^2-bonded carbon in the aromatic cycles (N−C═N), C-NH_x on the edges of heptazine units and adventitious carbon species, respectively. It is noted that the 286.7 eV signal of SCN and MSCN are enhanced compared with BCN and attributed to the formation of cyano group (−C≡N) which has the similar binding energy with C-NH_x [19,33]. The N 1s XPS spectra (Fig. 3b) for BCN is deconvolved into three components at 398.6, 399.8, and 401.1 eV, ascribed to bicoordinated (C═N−C) and tricoordinated ($(C)_3$−N) nitrogen atoms and NH_x groups, respectively [37]. The binding energy of N 1s for MCN is shifted toward higher energy due to the formation of N–O band, and electron transfer from C_3N_4 to MnO_x [7,28]. For SCN, the peak positive shift confirms N atoms of C_3N_4 aromatic rings have a strong interaction with the donor-type Na ions [38,39]. The higher binding energy of N 1s for MSCN results from the synergistic effect of Na coordination and MnO_x. The Mn 2p spectra of MSCN (Fig. 3c) can be observed two peaks with the spin-orbital splitting of 11.6 eV located at 642.0 and 653.6 eV assigned to Mn $2p_{3/2}$ and Mn $2p_{1/2}$ respectively, which is in accordance with the reported Mn_3O_4 [40]. The O 1s spectra of MSCN (Fig. S4) demonstrates that the lattice oxygen (529.9 eV) is belong to Mn−O−Mn, while the others are attributed to surface adsorbed species. In Fig. 3d, the high-resolution spectra of Na 1s at 1071.4 eV, lower in energy than that of Na-O bonding and any sodium salt, is in accordance with the reported binding energy of NaN_3 as illustrated in inset [18,41]. Moreover, there is no Cl 2p signals in the high-resolution spectra of MSCN, which excludes the existence of NaCl because it is easy to be removed by washing (Fig. S6).

The photocatalytic performance of all samples were evaluated by photocatalytic hydrogen evolution under visible light irradiation ($\lambda > 420$ nm) with 10 vol% triethanolamine as the electron sacrificial agent and 3 wt% Pt as co-catalyst. As shown in Fig. 4a, BCN shows a low H_2 evolution rate of 58.6 μmol $h^{-1} g^{-1}$ due to the inherent quick electron-hole recombination, while the H_2 evolution rates of MCN and SCN are 231.6 and 313.2 μmol $h^{-1} g^{-1}$ with an enhancement by a factor of 4 and 5 over BCN, respectively. All the $MSCN_x$ samples with different MnO_x loads have higher performance compared to MCN and SCN (Fig. S7). In addition, we tested the effect of different calcination temperatures (Fig. S8). Remarkably, the MSCN fabricated with an initial dosage of 0.08 g manganese acetate and calcined at 520 °C exhibits the highest H_2 production activity of 1085.6 μmol $h^{-1} g^{-1}$, which is *ca.* 18 times higher than that of BCN. The used MSCN sample analyzed by

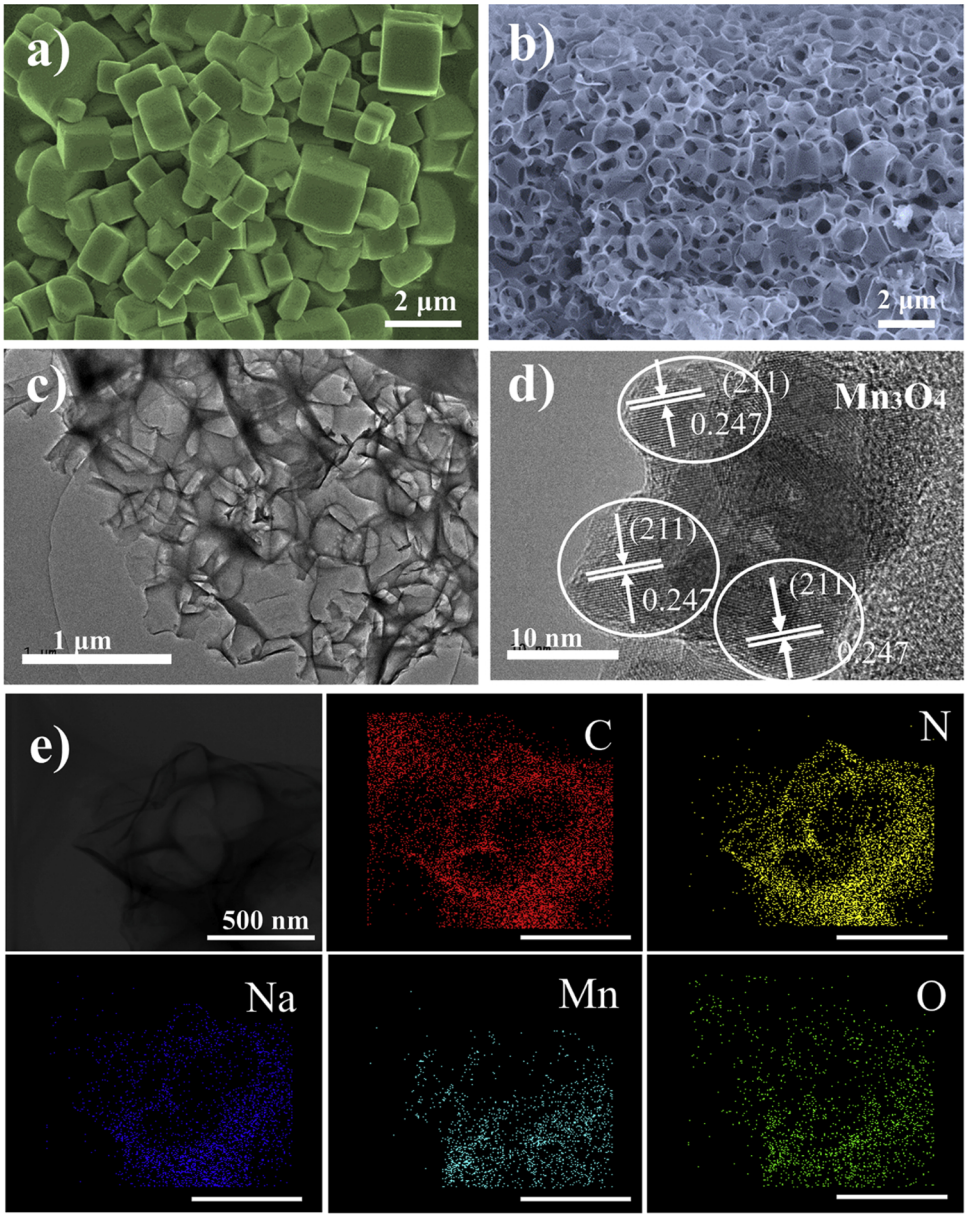

Fig. 1. SEM images of a) precursor@salt templates, b) MSCN, c) TEM images of MSCN, d) HRTEM images of MSCN, e) The corresponding elemental mapping of MSCN.

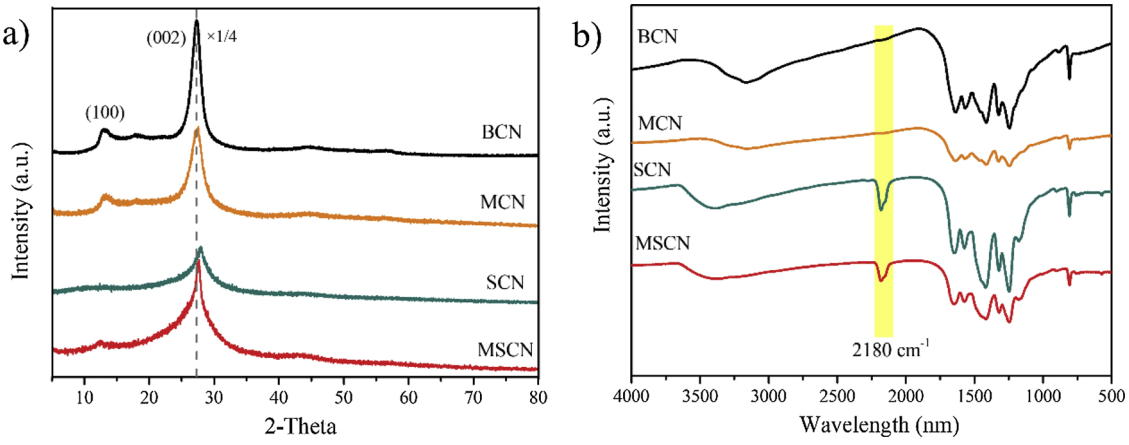

Fig. 2. a) XRD patterns and b) FT-IR spectra of BCN, SCN, MCN and MSCN.

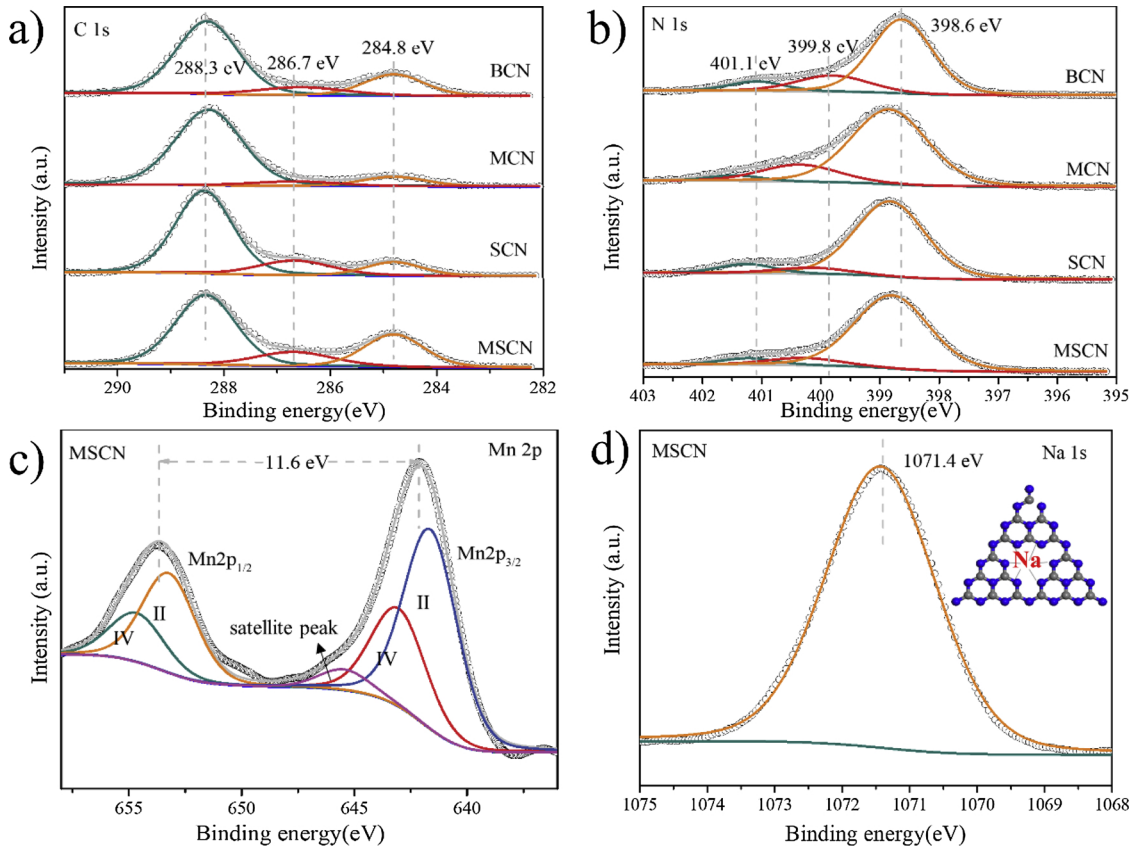

Fig. 3. (a) C 1s and (b) N 1s high-resolution XPS spectra of BCN, MCN, SCN and MSCN. (c) Mn 2 p and (d) Na 1s high-resolution spectra of MSCN.

SEM and XRD shows no obvious change of the morphology and crystal structures (Fig. S9). Meanwhile, no distinct activity decay is observed after 5 recycling runs (Fig. 4b), indicating the good photocatalytic stability.

As shown in Fig. 4a, the HER rate normalized by the surface area of MCN shows enhanced activity than that of BCN, indicating the MnO_x can promote charge separation due to inherent hole-trapping ability and then accelerate the oxidation reaction. The higher normalized activity of SCN confirms that NaCl templates can not only offer high surface area by pore-forming but also affect electronic structure. For MSCN, the excellent activity is ascribed to the synergistic effect of MnO_x decoration and NaCl treatment. The optical adsorption property were tested by UV–vis diffuse reflection spectra (DRS) in Fig. 5a. BCN shows a strong intrinsic absorption band at 460 nm which is consistent with previous literature [42]. The incorporation of Na elements or/and MnO_x endow SCN, MCN and MSCN with intensive visible light absorption, assigned to MnO_x decoration and Na coordination which forms the electronic states located within the band gap. The band gaps of BCN, MCN, SCN and MSCN are 2.74, 2.74, 2.71 and 2.67 eV, respectively (Fig. 5b). The valence band (VB) XPS are used to determine the VB edges as shown in Fig. 5c. It is obvious that the VB potential of MSCN shows a negative shift compared to BCN. According to the corresponding band gap and VB band potential, the conduction band (CB) can be deduced in Fig. 5d. The more negative conduction band of MSCN results in strong reduction ability in terms of thermodynamic requirements, which contributes to the H_2 production.

The behaviors of charge carriers, including excitation, intra-band relaxation, recombination and separation, are crucial to the photocatalytic performance. For MSCN the low-electronegativity sodium atoms have a weak interaction with lone-pair electrons, and act as an electron donor, while the cyano groups are electron withdrawing group and work as an electron acceptor. Therefore, this unique structure

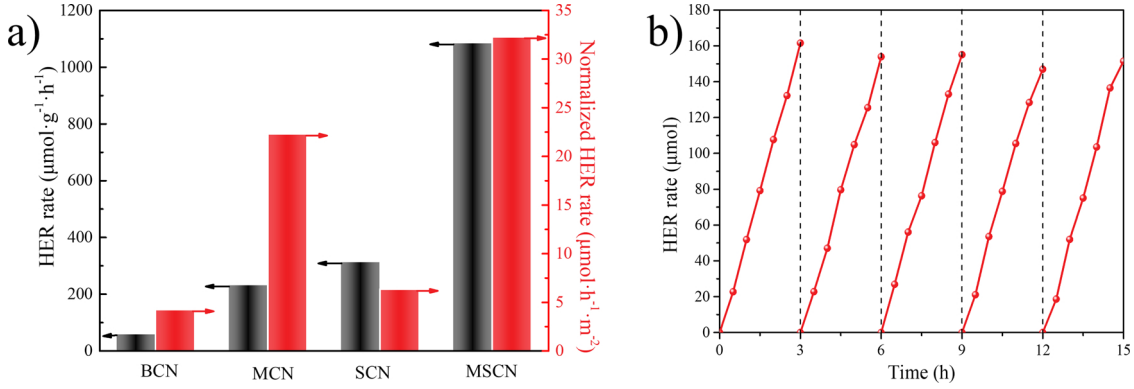

Fig. 4. (a) HER rate and Normalized HER rate of BCN, MCN, SCN and MSCN, (b) Cycling HER rate of MSCN under visible-light irradiation ($\lambda > 420$ nm).

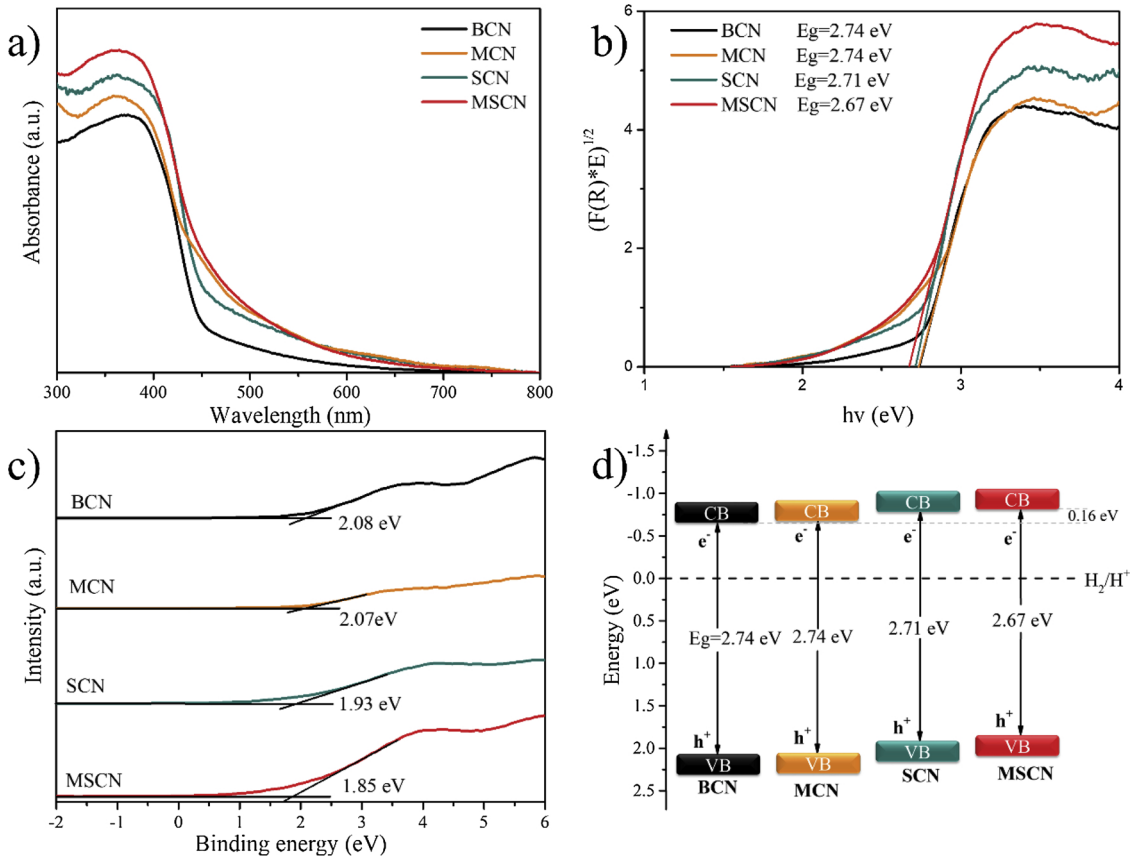

Fig. 5. (a) UV–vis absorption spectra, (b) Estimated band gaps through Kubelka–Munk function, (c) VB XPS, and (d) Schematic illustration of band structure of BCN, MCN, SCN and MSCN.

construct an internal donor–acceptor system, which promotes excitons dissociation and improves the photocatalytic activity [21]. MnO_x with the specific hole-trapping characteristics work as the additional driving force to accelerate charge separation. The photoluminescence (PL) spectra was measured to investigate the charge separation efficiency (Fig. 6a). BCN shows a strong emission peak at about 460 nm arising from delocalized π*-n radiative transition. The PL intensity of MCN, SCN and MSCN all decrease sharply after MnO_x-decorated or/and NaCl treatment, this indicates that the recombination of the photogenerated electrons and holes are suppressed. For BCN and MSCN, the PL lifetime of charge carriers was measured by the time-resolved PL spectra as shown in Fig. 6b. The detailed fitted lifetimes and their percentages are listed in Table S2. It is note that the average lifetime of MSCN (3.05 ns) is shorter than BCN (7.33 ns). The shorter lifetime of MSCN means that the energy relaxation is more likely to occur through nonradiative processes, that is, it will promote the photocatalytic H_2 production rate [43]. The EIS Nyquist plots and transient photocurrent response were further conducted with the open circuit potential (Fig. S10) to investigate the separation and migration of the light-induced electrons and holes in the photocatalysts. The smaller arc radius of three modified samples compared to BCN indicates the promotion of interfacial charge transfer achieved after modification (Fig. 6c). Especially, MSCN shows the lowest resistance and the most efficient separation of photogenerated charge carriers. Meanwhile, the photocurrent density of MSCN is nearly triple than BCN indicating that the migration of the charge carriers is more efficient (Fig. 6d). Such enhanced charge transfer efficiency is mainly attributed to the intramolecular D-A system and MnO_x for alleviating charge recombination.

Based on above measurements and analysis, the boosted photocatalytic activity of MSCN for hydrogen production can be explained as follows. First, the 3D porous structure obtained by salt-assisted strategy offer high surface area and provide more active sites. Second, Na doping and the accompanying cyano group are conducive to form an intramolecular D-A system for charge separation and stronger reduction ability for enhanced electron-related photocatalytic hydrogen evolution. Finally, MnO_x effectively trap holes for promoting charge separation and work as photocatalytic oxidation co-catalyst to enhance the photocatalytic activity.

4. Conclusions

We report a simple yet efficient salt-template-assisted method to fabricate MnO_x-decorated C_3N_4 to enhance the photocatalytic H_2 production activity. The NaCl templates simultaneously endow C_3N_4 with 3D open porous structure and a donor-acceptor structure by introducing Na coordination and associated cyano groups. MnO_x as hole-trapping sites effectively promote separation of charge carriers. The obtained photocatalyst processes high surface area, enhanced visible light-harvesting, effective charge separation and transfer. As a consequence, it shows a photocatalytic H_2 production rate of 18-fold higher than bulk C_3N_4 under visible light. This work provides a promising way to improve C_3N_4 performance from the perspectives of morphology, electronic structure and carrier behavior regulation.

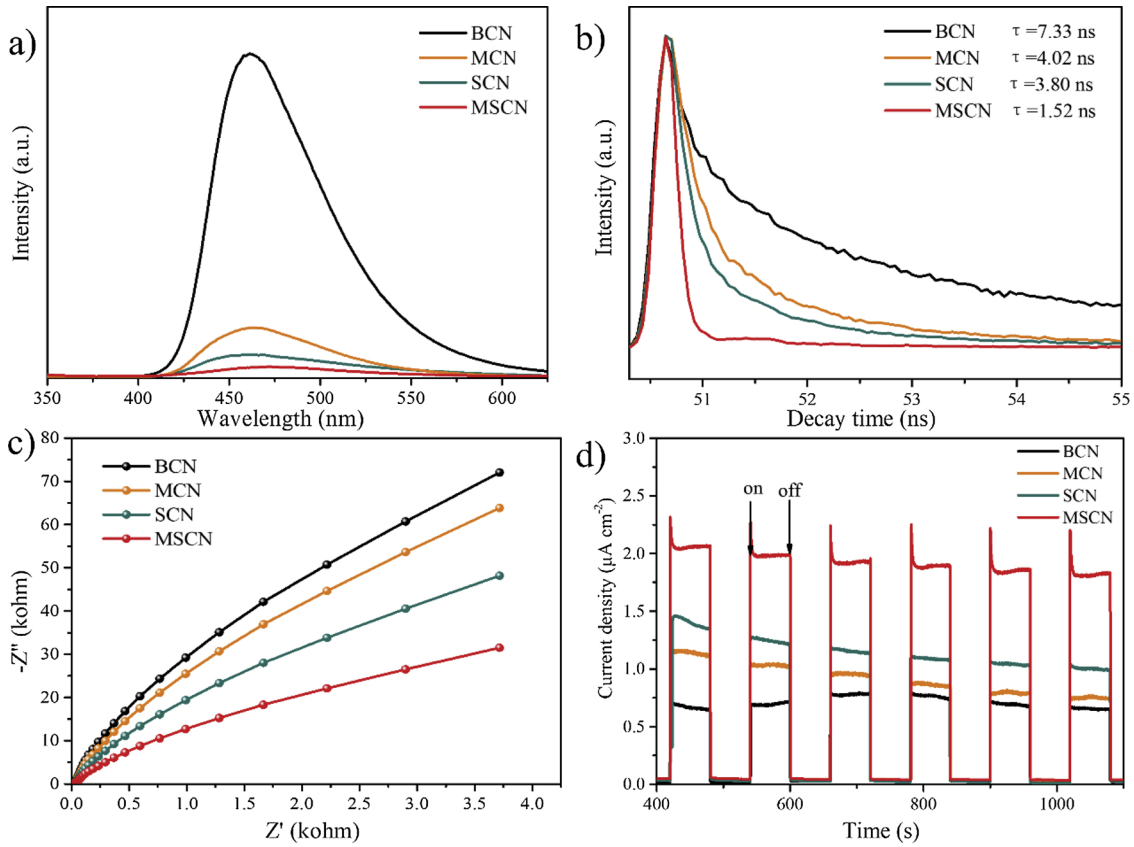

Fig. 6. (a) PL spectra and (b) Time-resolved PL decay spectra of BCN, MCN, SCN and MSCN. (c) EIS Nyquist plots and (d) Transient photocurrent responses of BCN, MCN, SCN and MSCN.

Acknowledgement

The authors appreciate the support from the National Natural Science Foundation of China (21676193, 51661145026).

Appendix A. Supplementary data

Supplementary material related to this article can be found, in the online version, at doi:https://doi.org/10.1016/j.apcatb.2019.117805.

References

[1] K. Mazloomi, C. Gomes, Hydrogen as an energy carrier: prospects and challenges, Renew. Sustain. Energy Rev. 16 (2012) 3024–3033.

[2] S. Chen, T. Takata, K. Domen, Particulate photocatalysts for overall water splitting, Nat. Rev. Mater. 2 (2017) 17050.

[3] Q. Xiang, B. Cheng, J. Yu, Graphene-based photocatalysts for solar-fuel generation, Angew. Chem. Int. Ed. 54 (2015) 11350–11366.

[4] Z.-F. Huang, J. Song, L. Pan, Z. Wang, X. Zhang, J.-J. Zou, W. Mi, X. Zhang, L. Wang, Carbon nitride with simultaneous porous network and O-doping for efficient solar-energy-driven hydrogen evolution, Nano Energy 12 (2015) 646–656.

[5] Z.-F. Huang, J. Song, X. Wang, L. Pan, K. Li, X. Zhang, L. Wang, J.-J. Zou, Switching charge transfer of C_3N_4 /$W_{18}O_{49}$ from type-II to Z-scheme by interfacial band bending for highly efficient photocatalytic hydrogen evolution, Nano Energy 40 (2017) 308–316.

[6] C. Marchal, T. Cottineau, M.G. Méndez-Medrano, C. Colbeau-Justin, V. Caps, V. Keller, Au/TiO_2–g-C_3N_4 nanocomposites for enhanced photocatalytic H_2 production from water under visible light irradiation with very low quantities of sacrifcial agents, Adv. Energy Mater. 8 (2018) 1702142.

[7] P. Xia, B. Zhu, B. Cheng, J. Yu, J. Xu, 2D/2D g-C_3N_4/MnO_2 nanocomposite as a direct Z-scheme photocatalyst for enhanced photocatalytic activity, ACS Sustain. Chem. Eng. 6 (2017) 965–973.

[8] Y. Kang, Y. Yang, L.C. Yin, X. Kang, L. Wang, G. Liu, H.M. Cheng, Selective breaking of hydrogen bonds of layered carbon nitride for visible light photocatalysis, Adv. Mater. 28 (2016) 6471–6477.

[9] D. Zhang, Y. Guo, Z. Zhao, Porous defect-modified graphitic carbon nitride via a facile one-step approach with significantly enhanced photocatalytic hydrogen evolution under visible light irradiation, Appl. Catal. B: Environ. 226 (2018) 1–9.

[10] Y. Zhang, M. Toshiyuki, J. Ye, A. Markus, Phosphorus-doped carbon nitride solid: enhanced electrical conductivity and photocurrent generation, J. Am. Chem. Soc. 132 (2010) 6294–6295.

[11] P.N. Gang Liu, C. Sun, Sean C. Smith, Z. Chen, G.Q. Lu, H.-M. Cheng, Unique electronic structure induced high photoreactivity of sulfur-doped graphitic C_3N_4, J. Am. Chem. Soc. 132 (2010) 11642–11648.

[12] Z. Ding, X. Chen, M. Antonietti, X. Wang, Synthesis of transition metal-modified carbon nitride polymers for selective hydrocarbon oxidation, ChemSusChem 4 (2011) 274–281.

[13] C.H. Choi, L. Lin, S. Gim, S. Lee, H. Kim, X. Wang, W. Choi, Polymeric carbon nitride with localized aluminum coordination sites as a durable and efficient photocatalyst for visible light utilization, ACS Catal. 8 (2018) 4241–4256.

[14] V.W. Lau, I. Moudrakovski, T. Botari, S. Weinberger, M.B. Mesch, V. Duppel, J. Senker, V. Blum, B.V. Lotsch, Rational design of carbon nitride photocatalysts by identification of cyanamide defects as catalytically relevant sites, Nat. Commun. 7 (2016) 12165.

[15] X. Chen, Y.-S. Jun, K. Takanabe, K. Maeda, K. Domen, X. Fu, M. Antonietti, X. Wang, Ordered mesoporous SBA-15 type graphitic carbon nitride: a semiconductor host structure for photocatalytic hydrogen evolution with visible light, Chem. Mater. 21 (2009) 4093–4095.

[16] H. Yan, Soft-templating synthesis of mesoporous graphitic carbon nitride with enhanced photocatalytic H_2 evolution under visible light, Chem. Commun. 48 (2012) 3430–3432.

[17] Z. Chen, S. Lu, Q. Wu, F. He, N. Zhao, C. He, C. Shi, Salt-assisted synthesis of 3D open porous g-C_3N_4 decorated with cyano groups for photocatalytic hydrogen evolution, Nanoscale 10 (2018) 3008–3013.

[18] F. Yang, D. Liu, Y. Li, L. Cheng, J. Ye, Salt-template-assisted construction of honeycomb-like structured g-C_3N_4 with tunable band structure for enhanced photocatalytic H_2 production, Appl. Catal. B: Environ. 240 (2019) 64–71.

[19] S.W. Yilong Yang, Yalong Jiao, Zhiliang Wang, Mu Xiao, Du Aijun, Yongli Li, Jinshu Wang, Lianzhou Wan, An unusual red carbon nitride to boost the photoelectrochemical performance of wide bandgap photoanodes, Adv. Funct. Mater. (2018) 1805698.

[20] X. Fan, L. Zhang, R. Cheng, M. Wang, M. Li, Y. Zhou, J. Shi, Construction of graphitic C_3N_4-Based intramolecular donor–acceptor conjugated copolymers for photocatalytic hydrogen evolution, ACS Catal. 5 (2015) 5008–5015.

[21] H. Ou, X. Chen, L. Lin, Y. Fang, X. Wang, Biomimetic donor-acceptor motifs in conjugated polymers for promoting exciton splitting and charge separation, Angew. Chem. Int. Ed. 57 (2018) 8729–8733.

[22] G. Zhang, L. Lin, G. Li, Y. Zhang, A. Savateev, S. Zafeiratos, X. Wang, M. Antonietti, Ionothermal synthesis of triazine-heptazine-based copolymers with apparent quantum yields of 60% at 420 nm for solar hydrogen production from "sea water",

Angew. Chem. Int. Ed. 57 (2018) 9372–9376.
[23] J. Liu, L. Qiu, R. Alessandri, X. Qiu, G. Portale, J. Dong, W. Talsma, G. Ye, A.A. Sengrian, P.C.T. Souza, M.A. Loi, R.C. Chiechi, S.J. Marrink, J.C. Hummelen, L.J.A. Koster, Enhancing molecular n-type doping of donor-acceptor copolymers by tailoring side chains, Adv. Mater. 30 (2018) 1704630.
[24] K. Li, W.D. Zhang, Creating graphitic carbon nitride based donor-π-acceptor-π-donor structured catalysts for highly photocatalytic hydrogen evolution, Small 14 (2018) e1703599.
[25] S. Sun, Y.-C. Zhang, G. Shen, Y. Wang, X. Liu, Z. Duan, L. Pan, X. Zhang, J.-J. Zou, Photoinduced composite of Pt decorated $Ni(OH)_2$ as strongly synergetic cocatalyst to boost H_2O activation for photocatalytic overall water splitting, Appl. Catal. B: Environ. 243 (2018) 253–261.
[26] A. Iwase, S. Yoshino, T. Takayama, Y.H. Ng, R. Amal, A. Kudo, Water splitting and CO_2 reduction under visible light irradiation using Z-scheme systems consisting of metal sulfides, CoO_x-loaded $BiVO_4$, and a reduced graphene oxide Electron mediator, J. Am. Chem. Soc. 138 (2016) 10260–10264.
[27] Y. Bai, L. Ye, L. Wang, X. Shi, P. Wang, W. Bai, A dual-cocatalyst-loaded Au/BiOI/MnO_x system for enhanced photocatalytic greenhouse gas conversion into solar fuels, Environ. Sci-Nano 3 (2016) 902–909.
[28] F. Raziq, L. Sun, Y. Wang, X. Zhang, M. Humayun, S. Ali, L. Bai, Y. Qu, H. Yu, L. Jing, Synthesis of large surface-area g-C_3N_4 comodified with MnO_x and Au-TiO_2 as efficient visible-light photocatalysts for fuel production, Adv. Energy Mater. 8 (2018) 1701580.
[29] J. Zhao, J. Nan, Z. Zhao, N. Li, J. Liu, F. Cui, Energy-efficient fabrication of a novel multivalence Mn_3O_4-MnO_2 heterojunction for dye degradation under visible light irradiation, Appl. Catal. B: Environ. 202 (2017) 509–517.
[30] Z. Chen, P. Sun, B. Fan, Q. Liu, Z. Zhang, X. Fang, Textural and electronic structure engineering of carbon nitride via doping with π-deficient aromatic pyridine ring for improving photocatalytic activity, Appl. Catal. B: Environ. 170–171 (2015) 10–16.
[31] M. Wu, J.M. Yan, X.N. Tang, M. Zhao, Q. Jiang, Synthesis of potassium-modified graphitic carbon nitride with high photocatalytic activity for hydrogen evolution, ChemSusChem 7 (2014) 2654–2658.
[32] Y. Kang, Y. Yang, L.C. Yin, X. Kang, G. Liu, H.-M. Cheng, An amorphous carbon nitride photocatalyst with greatly extended visible-light-responsive range for photocatalytic hydrogen generation, Adv. Mater. 27 (2015) 4572–4577.
[33] H. Yu, R. Shi, Y. Zhao, T. Bian, Y. Zhao, C. Zhou, G.I.N. Waterhouse, L.-Z. Wu, C.-H. Tung, T. Zhang, Alkali-assisted synthesis of nitrogen deficient graphitic carbon nitride with tunable band structures for efficient visible-light-driven hydrogen evolution, Adv. Mater. 29 (2017) 1605148.
[34] T. Xiong, W. Cen, Y. Zhang, F. Dong, Bridging the g-C_3N_4 interlayers for enhanced photocatalysis, ACS Catal. 6 (2016) 2462–2472.
[35] Y. Li, J. Qu, F. Gao, S. Lv, L. Shi, C. He, J. Sun, In situ fabrication of Mn_3O_4 decorated graphene oxide as a synergistic catalyst for degradation of methylene blue, Appl. Catal. B: Environ. 162 (2015) 268–274.
[36] G. Liu, G. Zhao, W. Zhou, Y. Liu, H. Pang, H. Zhang, D. Hao, X. Meng, P. Li, T. Kako, J. Ye, In situ bond modulation of graphitic carbon nitride to construct p-n homojunctions for enhanced photocatalytic hydrogen production, Adv. Funct. Mater. 26 (2016) 6822–6829.
[37] Y. Hong, C. Li, D. Li, Z. Fang, B. Luo, X. Yan, H. Shen, B. Mao, W. Shi, Precisely tunable thickness of graphitic carbon nitride nanosheets for visible-light-driven photocatalytic hydrogen evolution, Nanoscale 9 (2017) 14103–14110.
[38] Z. Shu, Y. Wang, W. Wang, J. Zhou, T. Li, X. Liu, Y. Tan, Z. Zhao, A green one-pot approach for mesoporous g-C_3N_4 nanosheets with in situ sodium doping for enhanced photocatalytic hydrogen evolution, Int. J. Hydrogen Energy 44 (2019) 748–756.
[39] J. Jiang, S. Cao, C. Hu, C. Chen, A comparison study of alkali metal-doped g-C_3N_4 for visible-light photocatalytic hydrogen evolution, Chin. J. Catal. 38 (2017) 1981–1989.
[40] J. Duan, Y. Zheng, S. Chen, Y. Tang, M. Jaroniec, S. Qiao, Mesoporous hybrid material composed of Mn_3O_4 nanoparticles on nitrogen-doped graphene for highly efficient oxygen reduction reaction, Chem. Commun. 49 (2013) 7705–7707.
[41] W. Fang, J. Liu, L. Yu, Z. Jiang, W. Shangguan, Novel (Na, O) co-doped g-C_3N_4 with simultaneously enhanced absorption and narrowed bandgap for highly efficient hydrogen evolution, Appl. Catal. B: Environ. 209 (2017) 631–636.
[42] Y. Yu, W. Yan, W. Gao, P. Li, X. Wang, S. Wu, W. Song, K. Ding, Aromatic ring substituted g-C_3N_4 for enhanced photocatalytic hydrogen evolution, J. Mater. Chem. A 5 (2017) 17199–17203.
[43] J.-W. Zhang, S. Gong, N. Mahmood, L. Pan, X. Zhang, J.-J. Zou, Oxygen-doped nanoporous carbon nitride via water-based homogeneous supramolecular assembly for photocatalytic hydrogen evolution, Appl. Catal. B: Environ. 221 (2018) 9–16.